

WENO schemes on arbitrary unstructured meshes for laminar, transitional and turbulent flows



Panagiotis Tsoutsanis*, Antonios Foivos Antoniadis, Dimitris Drikakis

Department of Engineering Physics, Cranfield University, Cranfield MK43 0AL, United Kingdom

ARTICLE INFO

Article history:

Received 20 February 2013

Received in revised form 23 July 2013

Accepted 1 September 2013

Available online 11 September 2013

Keywords:

WENO
Unstructured
Hybrid mesh
ILES
Sphere
Turbulence
RANS
Hypersonic

ABSTRACT

This paper presents the development and implementation of weighted-essentially-non-oscillatory (WENO) schemes for viscous flows on arbitrary unstructured grids. WENO schemes up to fifth-order accurate have been implemented in conjunction with hybrid and non-hybrid unstructured grids. The schemes are investigated with reference to numerical and experimental results for the Taylor–Green vortex, as well as for laminar and turbulent flows around a sphere, and the turbulent shock-wave boundary layer interaction flow problem. The results show that the accuracy of the schemes depends on the arbitrariness of shape and orientation of the unstructured mesh elements, as well as the compactness of directional stencils. The WENO schemes provide a more accurate numerical framework compared to second-order and third-order total variation diminishing (TVD) methods, however, the fifth-order version of the schemes is computationally too expensive to make the schemes practically usable. On the other hand, the third-order variant offers an excellent numerical framework in terms of accuracy and computational cost compared to the fifth-order WENO and second-order TVD schemes. Parallelisation of the CFD code (henceforth labelled as UCNS3D), where the schemes have been implemented, shows that the present methods offer very good scalable performance.

Crown Copyright © 2013 Published by Elsevier Inc. All rights reserved.

1. Introduction

Unstructured meshes are currently used in several applications, including fluid dynamics, structural mechanics, acoustics, and seismology, amongst others, offering increased versatility in the application of computational fluid dynamics (CFD) methods in complex geometries.

High-order numerical methods for unstructured grids have been previously presented in different frameworks, including finite-volume (FV) [1–17]; discontinuous Galerkin (DG) [18–25]; and spectral finite-volume (SFV) [26–28]. Most research efforts have been spent in connection with unstructured tetrahedral meshes, however, in practical applications, e.g., viscous flows around/inside complex geometries, hybrid unstructured meshes consisting of different types of elements is preferred for accuracy and efficiency reasons. In the framework of FV methods, applications of hybrid unstructured meshes have been presented for steady [7] and unsteady (inviscid) flows [15,16], while in the DG framework, hybrid unstructured meshes have also been applied to (steady) viscous flows.

Previous studies have dealt with the development and application of essentially non-oscillatory (ENO) and weighted ENO (WENO) schemes to triangular and tetrahedral meshes in two and three dimensions [1,3,4,29–32] and, more recently, to hybrid unstructured meshes consisting of hexahedrals, tetrahedrals, prisms and pyramids for inviscid flows [15,16]. The

* Corresponding author.

E-mail addresses: panagiotis.tsoutsanis@cranfield.ac.uk (P. Tsoutsanis), a.f.antoniadis@cranfield.ac.uk (A.F. Antoniadis), d.drikakis@cranfield.ac.uk (D. Drikakis).

successful implementation of WENO schemes in conjunction with hybrid unstructured meshes for inviscid flows [15,16] has motivated their extension to viscous flows, which is the subject of the present paper.

In particular, we are interested in developing the above schemes for implicit large eddy simulations (ILES) [33–39] (and references therein). These studies have shown that the built-in numerical dissipation of high-resolution/high-order schemes acts as a subgrid scale model accounting for the effects of the unresolved (turbulent) flow scales. Both explicit (classical LES) and implicit turbulence models have their strengths and weaknesses, but the implicit approach referred to as ILES, or Monotonically Implicit Large Eddy Simulation (MILES), has increasingly gained considerable interest [34–42].

In the present work, the accuracy of unstructured-grid-based WENO schemes is assessed with reference to numerical, direct numerical and large eddy simulations, and experimental results. The numerical implementation of the schemes is independent of element shapes and can be applied to any type of unstructured grids. Section 2 presents the governing equations employed in this study. In Section 3 the stencil and WENO construction algorithms for the inviscid and viscous terms, the implementation near solid boundaries, and the temporal discretisation, are presented. The results from the application of the schemes to the Taylor–Green vortex problem, flows around a sphere and shock-wave boundary layer interaction flow problem are discussed in Section 4 and the conclusions drawn from the present study are presented in Section 5.

2. Governing equations

The numerical developments presented in this paper concern the three-dimensional, compressible Navier–Stokes equations:

$$\frac{\partial}{\partial t} \mathbf{U} + \frac{\partial}{\partial x} (\mathbf{F}_c - \mathbf{F}_v) + \frac{\partial}{\partial y} (\mathbf{G}_c - \mathbf{G}_v) + \frac{\partial}{\partial z} (\mathbf{H}_c - \mathbf{H}_v) = 0 \quad (1)$$

where \mathbf{U} is the vector of the conservative variables; \mathbf{F}_c , \mathbf{H}_c , \mathbf{G}_c , and \mathbf{F}_v , \mathbf{G}_v , \mathbf{H}_v are the convective and viscous fluxes, respectively, in the x , y and z (Cartesian co-ordinate system) directions

$$\begin{aligned} \mathbf{U} &= \begin{bmatrix} \rho \\ \rho u \\ \rho v \\ \rho w \\ E \end{bmatrix}, & \mathbf{F}_c &= \begin{bmatrix} \rho u \\ \rho u^2 + p \\ \rho uv \\ \rho uw \\ u(E + p) \end{bmatrix}, & \mathbf{G}_c &= \begin{bmatrix} \rho v \\ \rho vu \\ \rho v^2 + p \\ \rho vw \\ v(E + p) \end{bmatrix}, \\ \mathbf{H}_c &= \begin{bmatrix} \rho w \\ \rho wu \\ \rho wv \\ \rho w^2 + p \\ w(E + p) \end{bmatrix}, & \mathbf{F}_v &= \begin{bmatrix} 0 \\ \tau_{xx} \\ \tau_{xy} \\ \tau_{xz} \\ \theta_x \end{bmatrix}, & \mathbf{G}_v &= \begin{bmatrix} 0 \\ \tau_{yx} \\ \tau_{yy} \\ \tau_{yz} \\ \theta_y \end{bmatrix}, & \mathbf{H}_v &= \begin{bmatrix} 0 \\ \tau_{zx} \\ \tau_{zy} \\ \tau_{zz} \\ \theta_z \end{bmatrix}. \end{aligned}$$

In the above, ρ is the density; u, v, w are the velocity components in x, y and z directions, respectively; p is the pressure; $E = p/(\gamma - 1) + (1/2)\rho(u^2 + v^2 + w^2)$ is total energy per unit mass; γ is the ratio of specific heats; τ_{ij} is the stress tensor; and θ is given by

$$\begin{aligned} \theta_x &= u\tau_{xx} + v\tau_{xy} + w\tau_{xz} + \frac{\mu\gamma}{Pr(\gamma - 1)} \frac{\partial T}{\partial x}, \\ \theta_y &= u\tau_{yx} + v\tau_{yy} + w\tau_{yz} + \frac{\mu\gamma}{Pr(\gamma - 1)} \frac{\partial T}{\partial y}, \\ \theta_z &= u\tau_{zx} + v\tau_{zy} + w\tau_{zz} + \frac{\mu\gamma}{Pr(\gamma - 1)} \frac{\partial T}{\partial z}. \end{aligned}$$

The perfect gas equation of state is also used with $\gamma = 1.4$; T is the temperature; Pr is the Prandtl number and the viscosity is related to temperature through the Sutherland law

$$\frac{\mu}{\mu_0} = \left(\frac{T}{T_0} \right)^{\frac{3}{2}} \frac{T_0 + S}{T + S}. \quad (2)$$

S is the Sutherland temperature and the subscript 0 denotes a reference state of the corresponding variables. The reference values are taken at atmospheric conditions (sea level) with $\mu_0 = 1.7894 \times 10^{-5}$ kg/(ms), $T_0 = 288.16$ K, $S = 110.4$ K and $Pr = 0.72$.

The spatial domain is discretised by conforming elements V_i of volume $|V_i|$. Integrating (1) over a mesh element the following semi-discrete finite-volume formulation is obtained

$$\frac{d}{dt} \mathbf{U}_i + \frac{1}{|V_i|} \oint_{\partial V_i} (\mathbf{F}_n^c - \mathbf{F}_n^v) dA = 0 \quad (3)$$

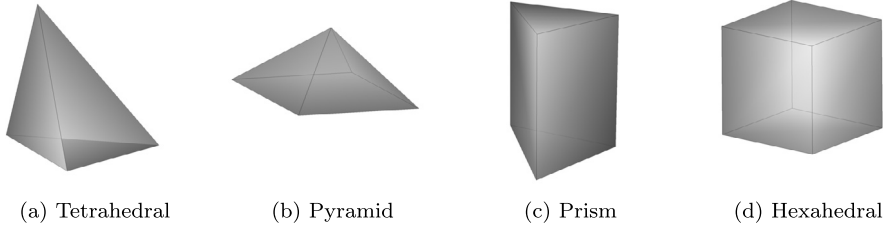


Fig. 1. Different types of mesh element shapes.

where $\mathbf{F}_n^c - \mathbf{F}_n^v$ are the projections of the convective and viscous flux vectors normal to the faces given by

$$\mathbf{F}_n^c = \begin{bmatrix} \rho V_n \\ \rho u V_n + n_x p \\ \rho v V_n + n_y p \\ \rho w V_n + n_z p \\ V_n(E + p) \end{bmatrix}, \quad \mathbf{F}_n^v = \begin{bmatrix} 0 \\ n_x \tau_{xx} + n_y \tau_{xy} + n_z \tau_{xz} \\ n_x \tau_{yx} + n_y \tau_{yy} + n_z \tau_{yz} \\ n_x \tau_{zx} + n_y \tau_{zy} + n_z \tau_{zz} \\ n_x \theta_x + n_y \theta_y + n_z \theta_z \end{bmatrix}$$

where A is the surface area of the corresponding face; $\mathbf{U}_i(t)$ is the conserved vector at time level t ; and V_n is the velocity normal to the surface area, A , defined by $V_n = n_x u + n_y v + n_z w$. Assuming that the surface of the element consists of L faces and denoting by \mathbf{n}_j the outward unit vector for a face A_j , then the integral over the element boundary ∂V_i splits into the sum of integrals over each face resulting in

$$\frac{d}{dt} \mathbf{U}_i = \mathbf{R}_i, \quad (4)$$

with

$$\mathbf{R}_i = -\frac{1}{|V_i|} \sum_{j=1}^L \int_{A_j} \mathbf{F}_{n,j}^c dA + \frac{1}{|V_i|} \sum_{j=1}^L \int_{A_j} \mathbf{F}_{n,j}^v dA.$$

A suitable Gaussian numerical quadrature is employed for the approximation of the integral expressions of the fluxes as shown below:

$$\int_{A_j} \mathbf{F}_{n,j}^c dA = \sum_{\alpha} \mathbf{F}_{n,j}^c(\mathbf{U}(\mathbf{x}_{\alpha}, t)) \omega_{\alpha} |A_j|, \quad (5)$$

$$\int_{A_j} \mathbf{F}_{n,j}^v dA = \sum_{\alpha} \mathbf{F}_{n,j}^v(\mathbf{U}(\mathbf{x}_{\alpha}, t)) \omega_{\alpha} |A_j|. \quad (6)$$

The subscript α corresponds to different Gaussian integration points \mathbf{x}_{α} and weights ω_{α} over the face. The calculation of the numerical convective and viscous fluxes of (5) and (6) requires the knowledge of the point-wise values of the conserved vector and the velocity and temperature gradients at each Gaussian integration point. Therefore, an interpolation procedure (reconstruction) must be used to obtain these values and this is an important building-block for achieving high-order of spatial accuracy. Different reconstruction techniques are utilised for the convective and viscous parts and these are presented in the next section.

3. Numerical framework

3.1. Spatial discretisation of convective terms

The spatial domain $\Omega \subset R^3$ is discretised into N number of conforming elements V_i with the index i ranging from 1 to N . The elements can be any combination of hexahedrals, pyramids, prisms, and tetrahedrals (Fig. 1).

The data in each element V_i is represented by cell averages of the conserved variable $u(x, y, z)$ as shown below

$$\bar{u}_i = \frac{1}{|V_i|} \int_{V_i} u(x, y, z) dV. \quad (7)$$

High-order of accuracy is attained by performing an interpolation (reconstruction) utilising the cell averages in such a way that a high-order approximation of point-wise values of the solution is achieved. The main task of the reconstruction is for

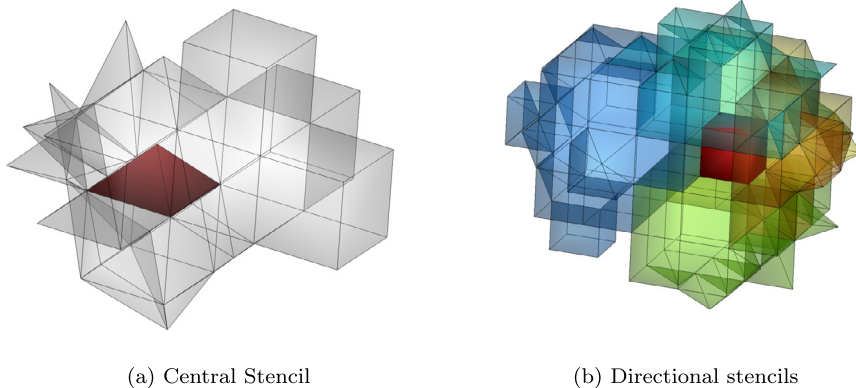


Fig. 2. Stencils. (For interpretation of the references to colour in this figure, the reader is referred to the web version of this article.)

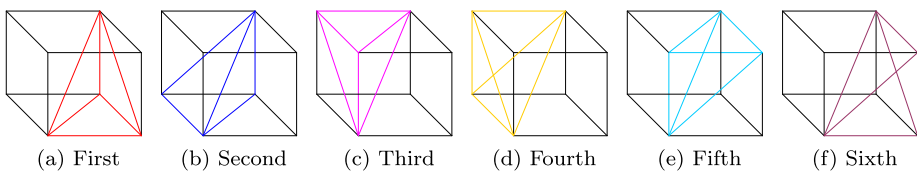


Fig. 3. Hexahedral decomposition.

each considered cell V_0 to build a high-order polynomial $p_i(x, y, z)$ that has the same cell average as u in the considered cell

$$\bar{u}_i = \frac{1}{|V_i|} \int_{V_i} u(x, y, z) dV = \frac{1}{|V_i|} \int_{V_i} p_i(x, y, z) dV. \quad (8)$$

Hence, a polynomial of any desired order of accuracy r is engaged to obtain the point-wise values of the conserved variable u in each cell. For this purpose the cell averages of $u(x, y, z)$ on the considered cell V_i , as well as the averages \bar{u}_m from the cells in the close spatial proximity, are used to perform the reconstruction. The union of the cells used to perform the reconstruction is named stencil.

The WENO reconstruction employs a central stencil and several directional stencils. The number of directional stencils is dependent upon the shape of the considered cell, the geometrical conditions applied, and they are always less or equal to the total number of faces of the target cell. The central stencil is built by recursively adding the direct side neighbours of the considered cell, until a number of elements in the stencil is reached. This process also applies to the directional stencils with the main difference being that a series of geometrical conditions must also be satisfied. The geometrical condition that must be satisfied is that the candidate element must lie within a specified geometrical sector defined by the planes arising from the vertices of the faces and the barycenter of the considered cell. However, the number of directional stencils becomes smaller under the presence of solid boundaries. The reader should refer to [16] for a detailed description of the geometrical conditions. Typical examples of a central stencil and a set of directional stencils in three-dimensions is shown in Fig. 2, where the considered cell, i , is illustrated in red colour.

3.1.1. Reconstruction basics

The main difficulty in obtaining a robust reconstruction that can achieve a desired order of accuracy is to minimise scaling effects occurring due to the different size and shape of the cells that make a stencil. A widely used approach is to employ inverse distance weights for the stencils reconstruction [13]. However, this has several limitations in curved boundaries as well as in cells with very high aspect ratio, which are encountered in the boundary layer region in viscous flows. Therefore, the reconstruction process adopted in this study is similar to [16,43], which removes any scaling effects by transforming the stencils from the physical space to a reference space.

Each target cell i that is not a tetrahedral is decomposed into tetrahedral elements. Particular attention must be paid in the way that elements, generated through an octree method, are decomposed [44,45]. The target cell and the elements in each stencil are transformed from the Cartesian co-ordinates (x, y, z) into a reference space described by (ξ, η, ζ) based on the Jacobian of one of the decomposed elements of the target cell. In the present study hexahedrals are decomposed in six tetrahedrals, the prisms in three tetrahedrals and pyramids in two tetrahedrals as shown in Figs. 3 and 4.

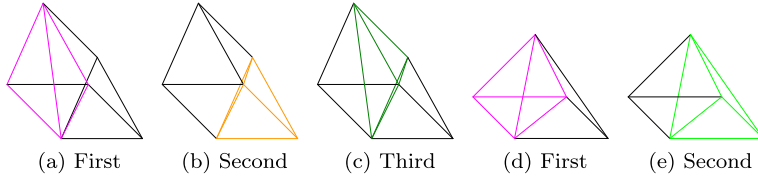


Fig. 4. Prism and pyramid decomposition.

Denoting the vertices of the target cell by \mathbf{v}_{ij} , $j = 1, 2, \dots, J_i$ and $\mathbf{w}_1 = (x_1, y_1, z_1)$, $\mathbf{w}_2 = (x_2, y_2, z_2)$, $\mathbf{w}_3 = (x_3, y_3, z_3)$ and $\mathbf{w}_4 = (x_4, y_4, z_4)$ the four vertices of one of the decomposed tetrahedral elements, the transformation from the Cartesian co-ordinates into the reference space is given by:

$$\begin{pmatrix} x \\ y \\ z \end{pmatrix} = \begin{pmatrix} x_1 \\ y_1 \\ z_1 \end{pmatrix} + J \cdot \begin{pmatrix} \xi \\ \eta \\ \zeta \end{pmatrix} \quad (9)$$

with the Jacobian matrix

$$J = \begin{bmatrix} x_2 - x_1 & x_3 - x_1 & x_4 - x_1 \\ y_2 - y_1 & y_3 - y_1 & y_4 - y_1 \\ z_2 - z_1 & z_3 - z_1 & z_4 - z_1 \end{bmatrix}. \quad (10)$$

Applying the inverse mapping, the element V_i can be transformed to the element V'_i in the reference co-ordinate system

$$\mathbf{v}'_{ij} = J^{-1} \cdot (\mathbf{v}_{ij} - \mathbf{w}_1), \quad j = 1, 2, \dots, J_i. \quad (11)$$

It is noted, that during the transformation the spatial average of $u(x, y, z)$ in each cell does not change

$$\bar{u}_i = \frac{1}{|V_i|} \int_{V_i} u(x, y, z) dV \equiv \frac{1}{|V'_i|} \int_{V'_i} u(\xi, \eta, \zeta) d\xi d\eta d\zeta. \quad (12)$$

For the target element V_i , the reconstruction stencil \mathcal{S} is formed by $M + 1$ elements, including the target element V_i :

$$\mathcal{S} = \bigcup_{m=0}^M V_m. \quad (13)$$

The index m refers to the local numbering of the elements in the stencil, with the index 0 corresponding to the target cell i . The r th order reconstruction polynomial at the transformed cell V'_0 is an expansion over local polynomial basis functions $\phi_k(\xi, \eta, \zeta)$:

$$p(\xi, \eta, \zeta) = \sum_{k=0}^K a_k \phi_k(\xi, \eta, \zeta) = \bar{u}_0 + \sum_{k=1}^K a_k \phi_k(\xi, \eta, \zeta) \quad (14)$$

where a_k are the degrees of freedom and the upper index, K , in the summation of the expansion, is related to the order of the polynomial r through the formula $K = \frac{1}{6}(r+1)(r+2)(r+3) - 1$. The most crucial requirement is that the basis functions must have zero mean value over the cell V'_0 in order to satisfy the conservation condition (7) since the transformed hexahedral, prisms or pyramids do not always correspond to a unit hexahedral, prism or pyramid. Therefore, the basis functions ϕ_k should be constructed in such a way that the conservation condition is satisfied identically irrespective of the degrees of freedom. The basis functions are defined as:

$$\phi_k(\xi, \eta, \zeta) \equiv \psi_k(\xi, \eta, \zeta) - \frac{1}{|V'_0|} \int_{V'_0} \psi_k d\xi d\eta d\zeta, \quad k = 1, 2, \dots. \quad (15)$$

Any type of type of orthogonal polynomial basis function can be utilised, and in the present study the shifted Legendre polynomial basis functions in the interval $[0, 1]$ were employed. In order to find the unknown degrees of freedom a_k , it must be satisfied that for each cell V'_m from the stencil the cell average of the reconstruction polynomial $p(\xi, \eta, \zeta)$ should be equal to the cell average of the solution \bar{u}_m :

$$\int_{E'_m} p(\xi, \eta, \zeta) d\xi d\eta d\zeta = |V'_m| \bar{u}_0 + \sum_{k=1}^K \int_{V'_m} a_k \phi_k d\xi d\eta d\zeta = |V'_m| u_m, \quad m = 1, \dots \quad (16)$$

Denoting as A_{mk} the integrals of the basis function k over the cell m

$$A_{mk} = \int_{V'_m} \phi_k d\xi d\eta d\zeta, \quad b_m = |V'_m|(\bar{u}_m - \bar{u}_0)$$

the equations for the degrees of freedom a_k are given in matrix form by

$$\sum_{k=1}^K A_{mk} a_k = b_m, \quad m = 1, 2, \dots, M. \quad (17)$$

A Gaussian quadrature rule is applied for the calculation of the volume integrals on the left-hand side of (17). For computing the degrees of freedom a_k , at least K cells are needed in the stencil, apart from the target cell E_0 . Using the minimum possible number of cells in the stencil, $M = K$, it may produce an ill-conditioned system [5,8,16,43], hence, $M = 2 \cdot K$ is chosen that improves the robustness and does not have a substantial performance penalty [16,43]. The least-square reconstruction is obtained by seeking the minimum of the following functional

$$\mathcal{F} = \sum_{m=1}^M \left(\sum_{k=1}^K A_{mk} a_k - b_m \right)^2.$$

Minimisation of \mathcal{F} leads to a linear system for a_k

$$\sum_{k=1}^K C_k a_k = \sum_{m=1}^M A_{mp} b_m, \quad C_k = \left(\sum_{m=1}^M A_{mk} A_{mp} \right), \quad p = 1, \dots, K. \quad (18)$$

The resulting least-squares system is solved by a QR decomposition and the coefficients of the linear symmetric matrix A are precomputed and stored for each cell during the preprocessing stage of the calculation, hence, improving the computational efficiency of the method. By solving the least-squares system of equations the reconstruction polynomial (14) can then be computed.

3.1.2. WENO reconstruction

The key ingredient of the WENO reconstruction is the non-linear, solution-adaptive combination of reconstruction polynomials arising from several different stencils [30,31,46]. The non-linear weights are determined by linear (constant) weights taking into account the smoothness of the solution in each of the reconstruction stencils. The WENO reconstruction is characterised by high-order of accuracy in smooth regions of the flow and non-oscillatory behaviour in regions with sharp gradients. It is defined as a non-linear combination of reconstruction polynomials $p_m(\xi, \eta, \zeta)$ obtained by using individual stencils \mathcal{S}_m :

$$p_{\text{weno}} = \sum_{m=0}^{m_s} \omega_m p_m(\xi, \eta, \zeta). \quad (19)$$

Substituting the form of the individual polynomial (14) corresponding to the stencil \mathcal{S}_m

$$p_m(\xi, \eta, \zeta) = \sum_{k=0}^K a_k^{(m)} \phi_k(\xi, \eta, \zeta) \quad (20)$$

and applying the condition for the total sum of the weights being equal to unity, it yields

$$p_{\text{weno}} = \sum_{m=0}^{m_s} \omega_m \left(\sum_{k=0}^K a_k^{(m)} \phi_k(\xi, \eta, \zeta) \right) = \bar{u}_0 + \sum_{m=0}^{m_s} \omega_m \left(\sum_{k=1}^K \tilde{a}_k \phi_k(\xi, \eta, \zeta) \right). \quad (21)$$

Rearranging the above formula gives

$$p_{\text{weno}} = \bar{u}_0 + \sum_{k=1}^K \left(\sum_{m=0}^{m_s} \omega_m a_k^{(m)} \right) \phi_k(\xi, \eta, \zeta) \equiv \bar{u}_0 + \sum_{k=1}^K \tilde{a}_k \phi_k(\xi, \eta, \zeta) \quad (22)$$

where ω_m are the non-linear weights and \tilde{a}_k are the reconstructed degrees of freedoms. The approach of [3,16] is adopted for the definition of the non-linear weights ω_m [3,16]

$$\omega_m = \frac{\gamma_m}{\sum_{m=0}^{m_s} \gamma_m}, \quad \gamma_m = \frac{d_m}{(\varepsilon + IS_m)^p}$$

where IS_m indicates how smooth the solution is on the stencil; d_m is the linear weights and ε is a small number used to avoid division by zero. In the present study, the central stencil is assigned a large linear weight, $d_0 = 10^3$, whereas the sectorial stencils are assigned smaller weights $d_m = 1$. The typical value used for ε is 10^{-6} and $p = 4$; for more details see [43]. The smoothness indicators IS_m can be computed in a mesh-independent manner as

$$IS_m = \sum_{\substack{1 \leq |\beta| \leq r \\ V'_0}} \int_{V'_0} (D^\beta p_m(\xi, \eta, \zeta))^2 d\xi d\eta d\zeta \quad (23)$$

where β is a multi-index [12,13,46], r is the order of the polynomial and D is the derivative operator. Since the smoothness indicators are quadratic functions of the degrees of freedom $a_k^{(m)}$, they can be expressed in terms of the universal oscillation indicator matrix [3].

In order to enhance the robustness and non-oscillatory properties of the scheme, the WENO reconstruction is carried out in characteristic variables [30,47]. The WENO characteristics reconstruction procedure utilises for each face A_j of a considered cell i the normal vector n_j as the characteristic direction [3,16]. Defining an arithmetic average of the conserved vectors \mathbf{U}_i and $\mathbf{U}_{i'}$ of its adjacent neighbouring cell, sharing the face A_j , $\mathbf{U}'_n = \frac{1}{2}(\mathbf{U}_i + \mathbf{U}_{i'})$, the left \mathbf{L}_j and right eigenvectors \mathbf{R}_j of the Jacobian matrix \mathbf{H}_j are computed, with the Jacobian matrix being the normal projection of the flux tensor calculated at this average state $\mathbf{H}_j = \frac{\partial \mathbf{F}_n}{\partial \mathbf{U}}|_{\mathbf{U}=\mathbf{U}'_n}$. The characteristic projections of the vector of the degrees of freedom of each stencil S_m , including the cell averaged value $\bar{\mathbf{U}}_i$, are computed as

$$\mathbf{B}_{ikj}^{(m)} = \mathbf{L}_j \mathbf{A}_{ik}^{(m)}, \quad m = 0, \dots, m_s, \quad k = 0, \dots, K. \quad (24)$$

The WENO reconstruction is employed for each component of the projected degrees of freedom and after that the reconstructed degrees of freedom $\tilde{\mathbf{B}}_{ikj}^{(m)}$ are projected back by multiplying them with the right eigenvector \mathbf{R}_j , hence, the WENO reconstruction polynomial reads

$$\mathbf{P}_{ij}(\xi, \eta, \zeta) = \bar{\mathbf{U}}_i + \sum_{k=1}^K \tilde{\mathbf{A}}_{ikj} \phi_{ik}(\xi, \eta, \zeta), \quad \tilde{\mathbf{A}}_{ikj} = \mathbf{R}_j \mathbf{B}_{ikj}. \quad (25)$$

The reconstructed values at each Gaussian integration points $(\xi_\beta, \eta_\beta, \zeta_\beta)$ in the reference co-ordinate system of the face A_j of the cell V_i are obtained through the following expression

$$\mathbf{P}_i(\xi_\beta, \eta_\beta, \zeta_\beta) = \bar{\mathbf{U}}_i + \sum_{k=1}^K \mathbf{A}_{ikj} \phi_{ik}(\xi_\beta, \eta_\beta, \zeta_\beta). \quad (26)$$

Although the WENO scheme reconstructs the entire polynomials, it does not employ the ENO-type algorithm for the smoothest polynomial as in [3].

3.2. Spatial discretisation of the viscous terms

In order to calculate the viscous fluxes for each face A_j of a cell i , the boundary extrapolated values for the velocity ∇u and temperature ∇T gradients at each surface Gaussian integration point must be computed. The central least-square reconstruction utilising only the central stencil is employed, as described in Sections 3.1 and 3.1.1. The resulting reconstruction polynomials are employed for obtaining the spatial derivatives of the considered variable, as follows:

$$\begin{pmatrix} \frac{\partial u}{\partial x} \\ \frac{\partial u}{\partial y} \\ \frac{\partial u}{\partial z} \end{pmatrix}_i^j = (J^{-1})_i^T \begin{pmatrix} \frac{\partial p(\xi, \eta, \zeta)}{\partial \xi} \\ \frac{\partial p(\xi, \eta, \zeta)}{\partial \eta} \\ \frac{\partial p(\xi, \eta, \zeta)}{\partial z} \end{pmatrix}_i^j \quad (27)$$

where $(J^{-1})_i^T$ is the transpose of the inverse Jacobian defined in (10).

3.2.1. Special treatment at no-slip boundaries

A special treatment is applied to the calculation of the velocity and temperature spatial derivatives at no-slip wall boundaries to ensure that Dirichlet and Neumann boundary conditions are satisfied. The approach adopted in the present study is similar to [12,13]. For the velocity, at no-slip boundaries the following Dirichlet boundary condition applies:

$$\bar{u}_0 + \sum_{k=1}^K a_k \phi_k(x_\beta) = 0 \quad (28)$$

where x_β is the co-ordinate of a point at the no-slip bounded surface. Assuming that $\phi_1(x_\beta) \neq 0$ and eliminating a_1 gives

$$a_1 = -\frac{1}{\phi_1(x_\beta)} \left\{ \bar{u}_0 + \sum_{k=2}^K a_k \phi_k(x_\beta) \right\}. \quad (29)$$

Substituting (29) into (17) the least-square system takes the following form:

$$\sum_{k=2}^K \left\{ A_{mk} - \frac{A_{m1}\phi_k(x_\beta)}{\phi_1(x_\beta)} \right\} a_k = b_m + \frac{A_{m1}}{\phi_1(x_\beta)} \bar{u}_0. \quad (30)$$

For the temperature gradient at no-slip boundaries the following Neumann boundary condition applies:

$$\frac{\partial T}{\partial n} = n_x \frac{\partial T}{\partial x} + n_y \frac{\partial T}{\partial y} + n_z \frac{\partial T}{\partial z} = 0 \quad (31)$$

and can be formulated as follows

$$\sum_{k=1}^K a_k (n, \nabla \phi_k(x_\beta)) = 0. \quad (32)$$

Transforming the spatial derivative to the local co-ordinate system (ξ, η, ζ) according to (27) gives

$$(n, \nabla \phi_k(x_\beta)) = (n_x, n_y, n_z) (J^{-1})^T \begin{pmatrix} \frac{\partial \phi_k(x_\beta)}{\partial \xi} \\ \frac{\partial \phi_k(x_\beta)}{\partial \eta} \\ \frac{\partial \phi_k(x_\beta)}{\partial \zeta} \end{pmatrix} = (c_1, c_2, c_3) \times \begin{pmatrix} \frac{\partial \phi_k(x_\beta)}{\partial \xi} \\ \frac{\partial \phi_k(x_\beta)}{\partial \eta} \\ \frac{\partial \phi_k(x_\beta)}{\partial \zeta} \end{pmatrix}$$

where c_1, c_2, c_3 are given by

$$\begin{aligned} c_1 &= n_x (J^{-1})_{1,1}^T + n_y (J^{-1})_{2,1}^T + n_z (J^{-1})_{3,1}^T, \\ c_2 &= n_x (J^{-1})_{1,2}^T + n_y (J^{-1})_{2,2}^T + n_z (J^{-1})_{3,2}^T, \\ c_3 &= n_x (J^{-1})_{1,3}^T + n_y (J^{-1})_{2,3}^T + n_z (J^{-1})_{3,3}^T. \end{aligned}$$

Hence, the boundary condition (32) can be rewritten as

$$\sum_{k=1}^K a_k \varphi_k(x_\beta) = 0 \quad (33)$$

with

$$\varphi_k = c_1 \frac{\partial \phi_k(x_\beta)}{\partial \xi} + c_2 \frac{\partial \phi_k(x_\beta)}{\partial \eta} + c_3 \frac{\partial \phi_k(x_\beta)}{\partial \zeta}. \quad (34)$$

Assuming that $\phi_1(x_\beta) \neq 0$, eliminating a_1

$$a_1 = -\frac{1}{\varphi_1(x_\beta)} \left\{ \sum_{k=2}^K a_k \varphi_k(x_\beta) \right\} \quad (35)$$

and substituting (35) into (17) the least-square system takes the following form:

$$\sum_{k=2}^K \left\{ A_{mk} - \frac{A_{m1}\varphi_k(x_\beta)}{\varphi_1(x_\beta)} \right\} a_k = b_m. \quad (36)$$

Discretisations involving high-order surface approximations through Gaussian quadrature integration, result in a large number of Gaussian quadrature points on each surface, less than the degrees of freedom. Therefore, particular care must be taken, not to over-constrain the system of Eqs. (30) and (36) with simultaneous boundary constraints, thereby making the reconstruction process less robust [13]. In the present work, only the co-ordinates of the wall-bounded surface centre are utilised as constraints, thus increasing the overall efficiency of the algorithm.

3.3. Numerical fluxes

The point-wise values of the conserved vector \mathbf{U} , as well as the velocity (∇u) and temperature (∇T) gradients, are replaced by high-order reconstruction polynomials. Therefore, the convective and viscous fluxes for the face A_j of cell V_i are discontinuous at each Gaussian point β . For the convective numerical flux the values \mathbf{U}_β^- and \mathbf{U}_β^+ correspond to the reconstructed value of the cell V_i and its adjacent neighbour $V_{i'}$, respectively. The discontinuity at each Gaussian quadrature point is resolved by a monotone function of left and right boundary extrapolated values and the flux (5) can be rewritten as

$$\mathbf{K}_{ij} \approx \sum_\beta \tilde{\mathbf{F}}_{n,j}^\mathbf{c}(\mathbf{U}_\beta^-, \mathbf{U}_\beta^+) \omega_\beta |A_j|. \quad (37)$$

The HLLC Riemann solver of [48] has been employed to define $\tilde{\mathbf{F}}_{n,j}^\mathbf{c}(\mathbf{U}_\beta^-, \mathbf{U}_\beta^+)$.

The numerical viscous fluxes for the face A_j of cell V_i are given by:

$$\mathbf{F}_{n,j}^\mathbf{v} \approx \sum_\beta \tilde{\mathbf{F}}_{n,j}^\mathbf{v} \omega_\beta |A_j| \quad (38)$$

where

$$\tilde{\mathbf{F}}_{n,j}^\mathbf{v} = \begin{bmatrix} 0 \\ n_x \tilde{\tau}_{xx} + n_y \tilde{\tau}_{xy} + n_z \tilde{\tau}_{xz} \\ n_x \tilde{\tau}_{yx} + n_y \tilde{\tau}_{yy} + n_z \tilde{\tau}_{yz} \\ n_x \tilde{\tau}_{zx} + n_y \tilde{\tau}_{zy} + n_z \tilde{\tau}_{zz} \\ n_x \tilde{\theta}_x + n_y \tilde{\theta}_y + n_z \tilde{\theta}_z \end{bmatrix} \quad (39)$$

where $\tilde{\tau}_{ij}$ and $\tilde{\theta}$ are calculated by central averaging and, additionally,

$$\begin{aligned} \tilde{\mathbf{U}}_\beta &= \frac{1}{2}(\mathbf{U}_\beta^- + \mathbf{U}_\beta^+), \\ \nabla \tilde{\mathbf{u}}_\beta &= \frac{1}{2}(\nabla \mathbf{u}_\beta^- + \nabla \mathbf{u}_\beta^+), \\ \nabla \tilde{T}_\beta &= \frac{1}{2}(\nabla T_\beta^- + \nabla T_\beta^+). \end{aligned}$$

The superscripts $(-)$ and $(+)$ correspond to the boundary extrapolated value of cell V_i and its adjacent neighbour, $V_{i'}$, respectively. Although a number of highly sophisticated approaches for the treatment of viscous fluxes are available [21,25, 49], the central averaging approach was chosen for its simplicity and robustness.

3.4. Temporal discretisation

The TVD Runge–Kutta 3rd-order method has been employed for the temporal discretisation of the equations. This method provides high parallel performance and small memory footprint. For each cell i the solution is advanced in time as follows

$$\left. \begin{aligned} \mathbf{U}_i^1 &= \mathbf{U}_i^n + \Delta t \cdot \mathbf{R}_i(\mathbf{U}_i^n) \\ \mathbf{U}_i^2 &= \frac{3}{4} \mathbf{U}_i^n + \frac{1}{4} \mathbf{U}_i^1 + \frac{\Delta t}{4} \cdot \mathbf{R}_i(\mathbf{U}_i^1) \\ \mathbf{U}_i^{n+1} &= \frac{1}{3} \mathbf{U}_i^n + \frac{2}{3} \mathbf{U}_i^2 + \frac{2\Delta t}{3} \cdot \mathbf{R}_i(\mathbf{U}_i^2) \end{aligned} \right\} \quad (40)$$

where \mathbf{R}_i is given by (4).

The time step, Δt , is calculated by

$$\Delta t = K \frac{1}{\min_i \frac{S_i}{h_i} + \frac{1}{2} \frac{(\mu+k)}{h_i^2}} \quad (41)$$

where h_i is the radius of the inscribed sphere of each cell i , $K \leq 1/3$ is the CFL number for unsplit finite-volume schemes [48], μ is the dynamic viscosity, k is the thermal conductivity coefficient, and S_i is the maximum propagation speed in each cell i given by

$$S_i = sp_x \cdot n_x + sp_y \cdot n_y + sp_z \cdot n_z \quad (42)$$

Table 1

Mesh statistics for the Taylor–Green vortex.

	Hexa16	Hexa32	Hexa64	Tetra16	Tetra32	Tetra64
Elements <i>N</i>	Hexa 4096	Hexa 32,768	Hexa 262,144	Tetra 24,986	Tetra 198,901	Tetra 1,572,984

with

$$sp_x = |u| + a, \quad sp_y = |v| + a, \quad sp_z = |w| + a.$$

$\mathbf{n} = (n_x, n_y, n_z)$ is the outward unit normal vector, a is the speed of sound, and the characteristics are running inwards to the domain. For negative velocities, the local maximum of the eigenvalues is taken.

4. Applications

In this section, results from three unsteady applications employing the WENO schemes in three space dimensions using hexahedral, tetrahedral, prismatic and hybrid meshes, are presented.

4.1. Taylor–Green vortex

The first case features transition to turbulence in the Taylor–Green vortex (TGV). The TGV has been used as fundamental prototype for vortex stretching and consequent production of small-scale eddies, to address the basic dynamics of transition to turbulence based on DNS [50], as well as on ILES and classical LES (based on subgrid scale models) [51].

In the present study, the TGV has been selected to assess the dissipation rates of WENO schemes and their dependence upon the type of mesh. Similar to previous LES studies [51], the mesh size is considered significantly larger than the Kolmogorov scale, thus the simulations are performed using the 3D compressible Euler equations. The TGV is an incompressible flow that evolves from a two-dimensional initial velocity profile of the form:

$$u(x, 0) = \sin(kx) \cos(ky) \cos(kz), \quad (43)$$

$$v(x, 0) = -\cos(kx) \sin(ky) \cos(kz), \quad (44)$$

$$w(x, 0) = 0 \quad (45)$$

with density ρ and p pressure given by

$$\rho(x, 0) = 1, \quad (46)$$

$$p(x, 0) = 100 + \frac{\rho}{16} [\cos(2z) + 2 \cos(2x) + \cos(2y) - 2] \quad (47)$$

where $k = 2\pi/\lambda = 1$ is the wavenumber. The specified pressure constrains the flow to the incompressible regime with the Mach number being $M_\infty \approx 0.08$. The computational domain is defined by $(x, y, z) \in [0, 2\pi] \times [0, 2\pi] \times [0, 2\pi]$ with periodic boundary conditions. Simulations were carried out using the WENO-3rd and WENO-5th order schemes in conjunction with a constant unsplit finite-volume scheme and the TVD Runge–Kutta 3rd-order scheme with CFL number 0.28. Two different types of meshes were used consisting of hexahedral and tetrahedral elements as shown in Table 1 and Fig. 5, where N stands for the total number of elements. All the simulations were intentionally performed in under-resolved meshes, which is quite common for LES simulations at very high Reynolds numbers. The aim was to test the suitability of the numerical schemes employed and obtain physically meaningful results on coarse meshes. The simulations were run up to $t = 20$ s for obtaining the dissipation statistics.

In the incompressible limit, the kinetic energy can be damped by resolved (large scale) effects [42,52–54]. Since our aim is to employ the present numerical schemes without resorting to an explicit subgrid scale model, the behaviour of the dissipation mechanism with respect to different meshes is of interest. Although it might seem appealing to not use any form of limiting procedure in the reconstruction process for this low-Mach number incompressible test problem, our experience shows that the performance of a non-limited central stencil reconstruction in the framework of unstructured grids suffers from excessive dispersion errors, which may lead to unphysical results or abrupt termination of the simulation. This can be attributed to the fact that the large stencils of higher-order finite-volume schemes used in unstructured meshes, which in the case of the Taylor–Green vortex may span across regions of sharp velocity gradients, will lead to unphysical spurious oscillations. This problem is avoided by using WENO or MUSCL reconstruction schemes.

The volumetrically averaged kinetic energy decay in time is a way of quantifying the numerical dissipation of the schemes. This is plotted in Figs. 6 and 7 for hexahedral and tetrahedral meshes, respectively. Additionally, the results of Shu et al. [52] for the same test case using structured hexahedral meshes of various resolutions in conjunction with the WENO-5th order accurate scheme are included in the comparisons. The observations regarding the results are summarised below.

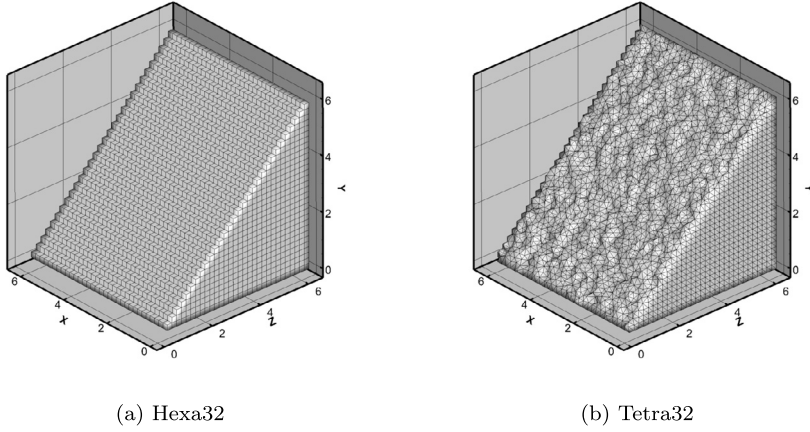


Fig. 5. Cutaway of the two meshes used in the Taylor–Green vortex flow simulations.

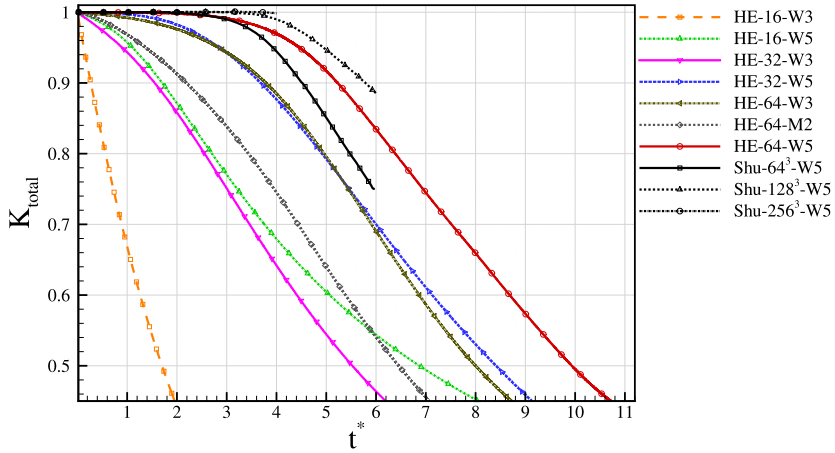


Fig. 6. Volumetrically averaged kinetic energy decay in time for the Taylor–Green vortex for hexahedral meshes ('W' and 'M' stand for WENO and MUSCL schemes, respectively); comparison with the results of Shu et al. [52] is also presented.

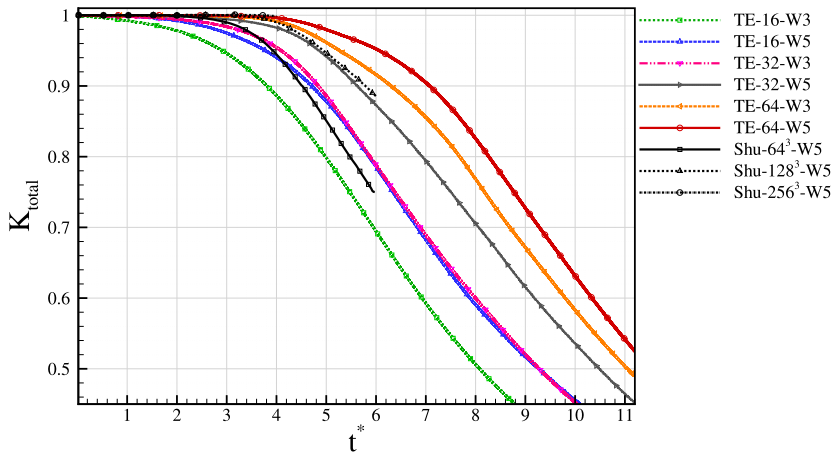


Fig. 7. Volumetrically averaged kinetic energy decay in time for the Taylor–Green vortex for tetrahedral meshes ('W' stands for WENO); comparison with the results of Shu et al. [52] is also included [52].

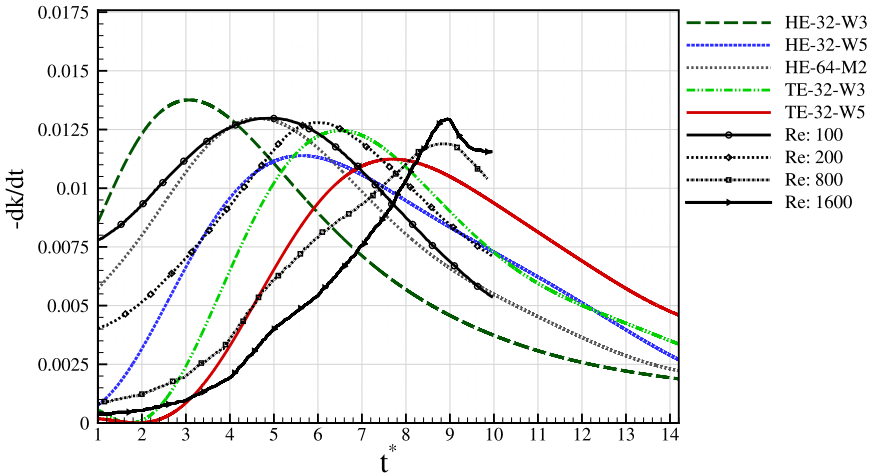


Fig. 8. Volumetrically averaged kinetic energy decay rate in time for the Taylor–Green vortex for different type of meshes at 32^3 resolution with various schemes ('W' and 'M' stand for WENO and MUSCL schemes, respectively); comparison with the DNS results of Brachet et al. [50] is also presented.

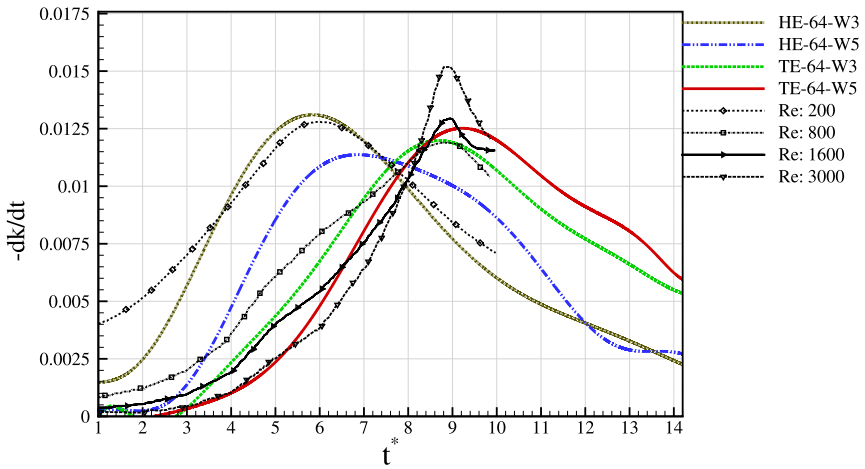


Fig. 9. Volumetrically averaged kinetic energy decay rate in time for the Taylor–Green vortex for different type of meshes at 64^3 resolution with various schemes ('W' stands for WENO); comparison with the DNS results of Brachet et al. [50] is also presented.

As the mesh resolution and the numerical order of accuracy increase, the numerical dissipation is reduced. The finest hexahedral mesh with the present WENO-5th provides less dissipative results than the structured hexahedral mesh and WENO-5th of Shu et al. [52] at the same mesh resolution. This is attributed to k-exact formulation of the WENO schemes used here, whereas in [52] the non-linear combination of lower-order reconstructions is used in conjunction with a Lax–Friedrichs flux splitting. The tetrahedral meshes outperform the hexahedral meshes, as well as the structured ones of [52] at higher resolutions. The main feature that significantly improves the efficiency and accuracy of the WENO schemes for the TGV case is that the tetrahedral stencils are more compact for the same order of accuracy compared to hexahedrals. Their arbitrary orientation with the axis is also beneficial for resolving the highly three-dimensional complicated flow features of the TGV problem. This conclusion is also supported by the results of the kinetic energy conservation error at $t = 6.0$ s (Fig. 10).

The factor that defines the successful implementation of a numerical scheme in the ILES context is its dissipation characteristics [35,51,53–59]. The inherited numerical dissipation and, consequently, the resolved physical viscosity (or corresponding Reynolds number) can be estimated by computing the evolution of the kinetic energy dissipation rate $-dK^*/dt^*$ and compare it with the DNS results of [50].

By closely examining the kinetic energy dissipation rates of Figs. 8 and 9, it is seen that as the mesh resolution and the numerical order of accuracy increase the kinetic energy dissipation rates approach the DNS results of [50] at higher Reynolds number, as also documented in [51] for a range of numerical methods.

The kinetic energy dissipation rates show that the results on tetrahedral meshes results correspond to higher Reynolds number DNS results of [50] than the hexahedral meshes, and this is attributed to their arbitrary orientation and stencils compactness. The 2nd-order MUSCL scheme [16] in conjunction with the Barth and Jespersen slope limiter on a 64^3 hex-

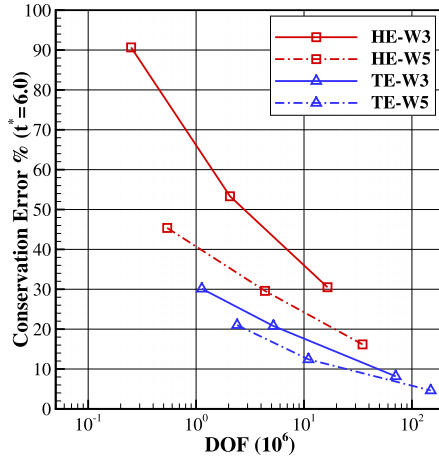


Fig. 10. Kinetic energy conservation error at time $t = 6.0$ s as function of the total number of degrees of freedom per mean flow variable for the Taylor-Green vortex.

ahedral mesh provides similar dissipation with the WENO-5th order scheme on a 32^3 hexahedral mesh using eight times less elements, as shown in Figs. 6 and 8.

In Fig. 11 the Q criterion [60] is used for the finest tetrahedral mesh with the WENO-5th scheme in order to track the time evolution of the Taylor–Green vortex problem showing the evolution of large structures to smaller scale organised vortices, followed by transition to fully developed turbulent flow.

4.2. Parallel scalability

The parallelisation performance of the present methods and computer code were investigated using the Taylor–Green vortex flow case in conjunction with the finest tetrahedral mesh resolution (1,572,984 elements). The METIS software [61] was used for grid partitioning. The numerical methods used in this paper were implemented in a Fortran 90 computer code called UCNS3D, which utilises the Message Passing Interface (MPI) for parallel communications. The parallel performance tests were conducted on the HECToR UK National Supercomputing Service facility.

The time required for one time-iteration of the WENO-3rd order scheme on 64 processors was used as a reference time to normalise the CPU results of the numerical simulations. To investigate the scalability of the methods and computer code, tests were performed with the number of processors varying from 64 to 8192.

When increasing the order of numerical accuracy the computational time increases faster than the communication time, thus higher-order numerical schemes scale better than lower-order schemes. This is illustrated in Fig. 12, where the WENO-5th order on 8192 processors gives a parallel efficiency of 84% and the WENO-3rd order scheme gives efficiencies of 83% and 63% on 2048 and 4096 processors, respectively.

Parallelisation of the unstructured WENO schemes requires communications between the processors for exchanging (i) the cell-centred values of every halo element on the stencil; (ii) the reconstructed, boundary extrapolated values of each Gaussian quadrature point of the direct-side halo neighbouring elements. The second communication requirement is common in high-order numerical schemes that employ high-order Gaussian quadrature approximations, such as structured and unstructured Finite-Volume schemes, DG, SFV etc. The amount of data required for (i) is far lower than (ii) because the latter involves the boundary extrapolated values of the solution and the solution gradients (for viscous flows) at each surface Gaussian quadrature point. For the WENO-5th order scheme, the exchange of the updated values of the stencil elements takes less than 4% of the total communication time on 8192 processors when the total communication time is 17% of the total CPU time. The wall-clock time taken per iteration for the WENO-3rd order scheme is 0.9 s on 64 processors of the HECTOR facility, and approximately one order of magnitude greater for the WENO-5th order scheme.

The numerical tests using the Taylor–Green vortex show that the best compromise between accuracy and computational cost is provided by the WENO-3rd order scheme. Therefore, the WENO-3rd order scheme was further employed in simulations of laminar and turbulent flow around a sphere.

4.3. Laminar flow past a sphere

The flow around a sphere at Reynolds number $Re = 300$ and free-stream Mach number $M_\infty = 0.5$ is an unsteady, laminar, non-axisymmetric, periodic flow featuring vortex shedding. The free-stream (non-dimensional) density and pressure are $\rho_\infty = 1$ and $p_\infty = 1/\gamma$, respectively. A hybrid unstructured mesh was utilised consisting of 675,464 elements, where the

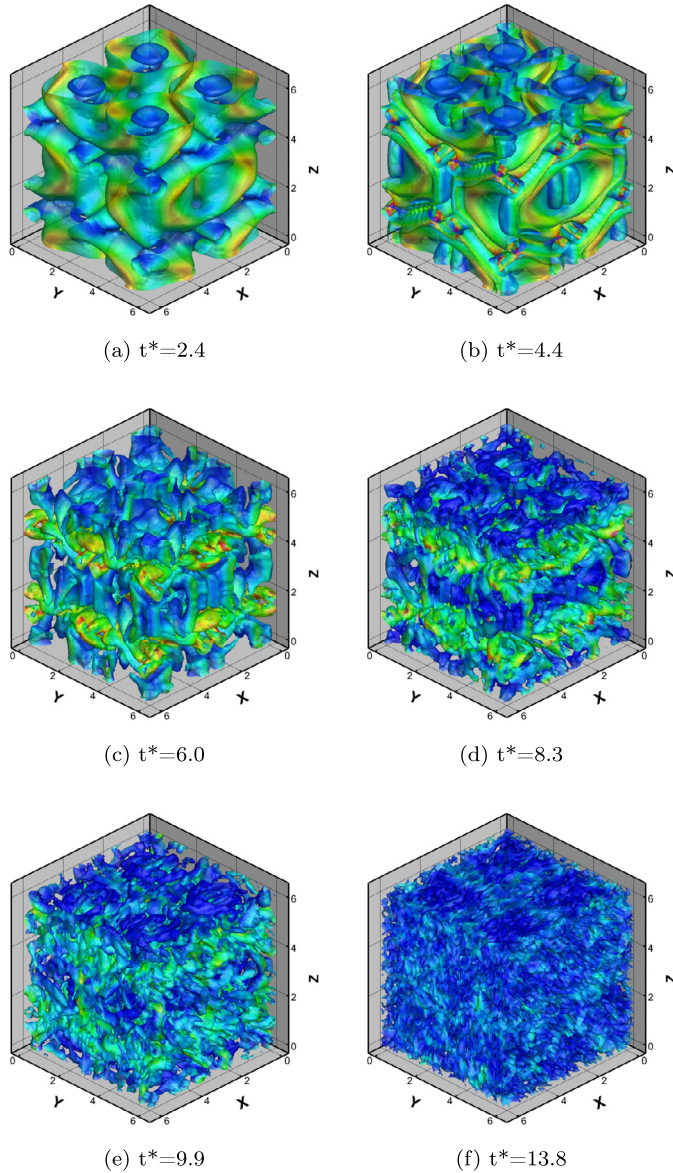


Fig. 11. Flow visualisation of the Taylor–Green vortex at various instants using the Q-criterion iso-surfaces (coloured by the kinetic energy) on the 64^3 tetrahedral mesh and the WENO-5th order scheme.

boundary layer region was discretised by prisms and the rest of the domain by tetrahedral elements Fig. 13. The computational domain has dimensions $(x, y, z) \in [0, 50] \times [0, 20] \times [0, 20]$, with the centre of the sphere located at $[10.5, 10, 10]$. No-slip was applied on the surface of the sphere and free-stream values elsewhere in the boundaries. The simulations were performed up to time $t = 282$ s, in order to obtain sufficient flow statistics, using the WENO-3rd in conjunction with the 3rd-order TVD Runge–Kutta and CFL = 0.28.

Fig. 14 shows the time histories of lift and drag coefficients. The average lift and drag coefficients are -0.061 and 0.653 , respectively, with the latter having an oscillation amplitude of 4.2×10^{-3} , which is in close agreement with the data of [62–65], and the references therein Table 2. It has to be noted that in the steady axisymmetric regime ($Re < 211$) the lift coefficient is naturally zero, but at the subject $Re = 300$ the recirculation eddy is not a closed bubble and the non-axisymmetry in the wake produces a lift force as it has been reported in experimental and computational studies in the literature [62,66]. The Strouhal number was calculated by monitoring the velocities in the wake of the sphere at $(15.5, 10, 10)$, see Fig. 15. The value of $St = 0.1356$ with a frequency of 8 oscillations over 118 s, was obtained, which is in close agreement with [62,63].

The vortical structures, including the hairpin structure, are shown in Fig. 16 using the Q criterion [60]. Simulations on the same grid resolution using the MUSCL-2nd order scheme, with the Barth and Jespersen slope limiter, showed that the

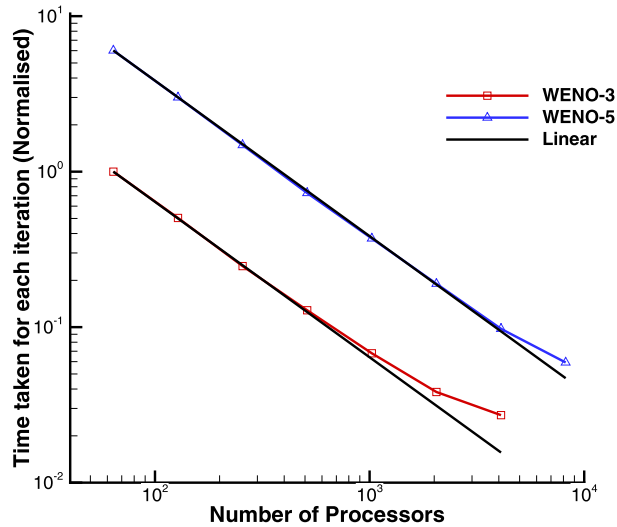
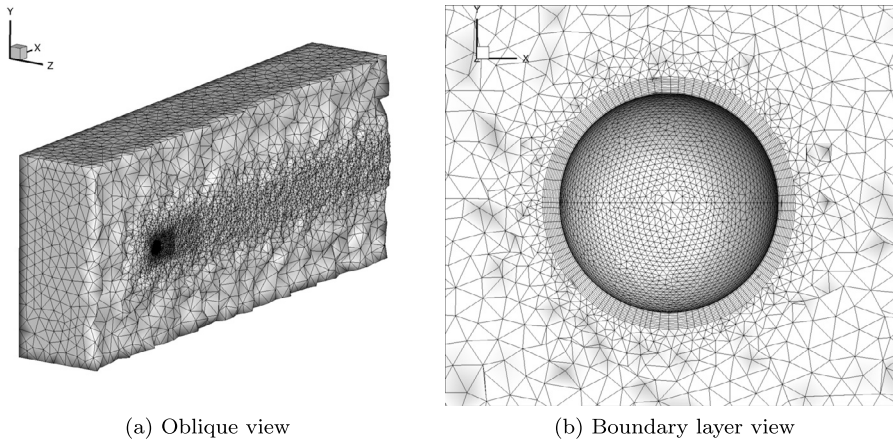


Fig. 12. Parallel scalability of WENO-5 and WENO-3 numerical schemes for the Taylor–Green vortex problem using the HECToR UK National Supercomputing Service facility.



(a) Oblique view

(b) Boundary layer view

Fig. 13. Cutaway of the unstructured mesh for the laminar flow past a sphere.

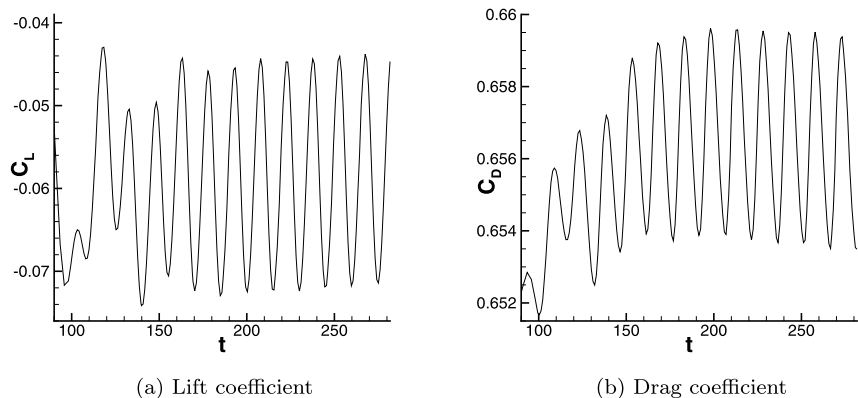
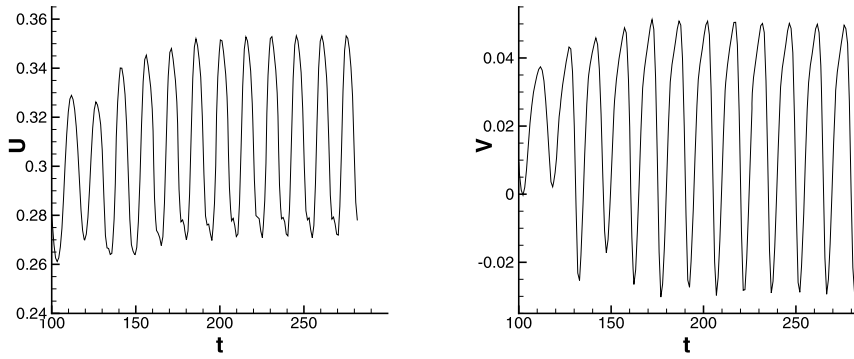


Fig. 14. Time histories of force coefficients for the laminar flow around a sphere.



(a) U (m/s) velocity variation in time at a selected position
(b) V (m/s) velocity variation with time at probe position

Fig. 15. Variation of U (m/s) and V (m/s) velocity in time at position (15.5, 10, 10) for the laminar flow around a sphere.

Table 2

Flow parameters at Reynolds = 300. Results from Johnson and Patel [62], Constantinescu and Squires [67] and Tomboulides and Orszag [63].

	C_D	C_L	Strouhal
Johnson and Patel [62]	0.656	-0.069	0.137
Tomboulides and Orszag [63]	0.671	-	0.136
Constantinescu and Squires [67]	0.655	0.065	0.136
Present	0.653	-0.061	0.1356

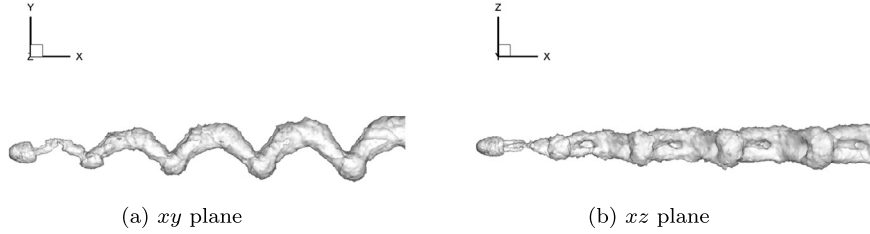


Fig. 16. Vortical structure at $t = 282$ s using the Q criterion for the laminar flow around a sphere.

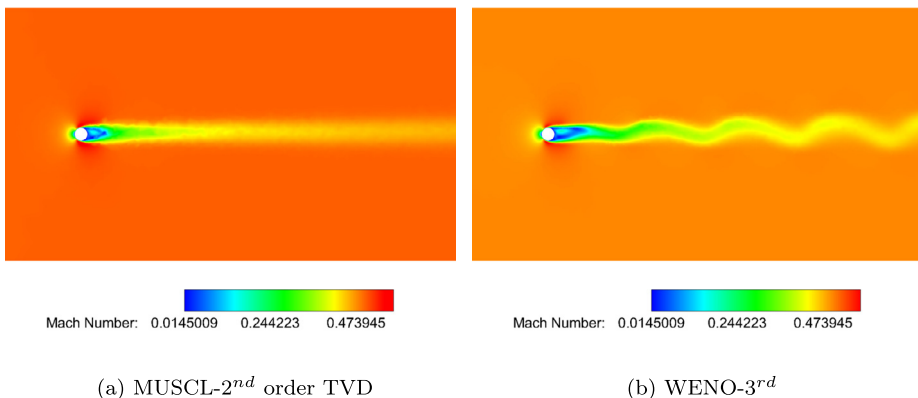


Fig. 17. Contour plots of Mach number at $t = 282$ s obtained with a MUSCL-2nd order TVD and a WENO-3rd order scheme for the laminar flow around a sphere.

2nd-order scheme was too dissipative to capture the unsteadiness in the wake of the sphere (Fig. 17). Finally, the oblique view of the vortical structures and iso-surfaces of the streamwise velocity (Fig. 18) show the non-axisymmetric nature of the flow. The high-resolution methods employed in the present study are essential for revealing the vortex shedding mechanism and the induced hairpin vortices, features that are not easy to visualise in experiments [62].

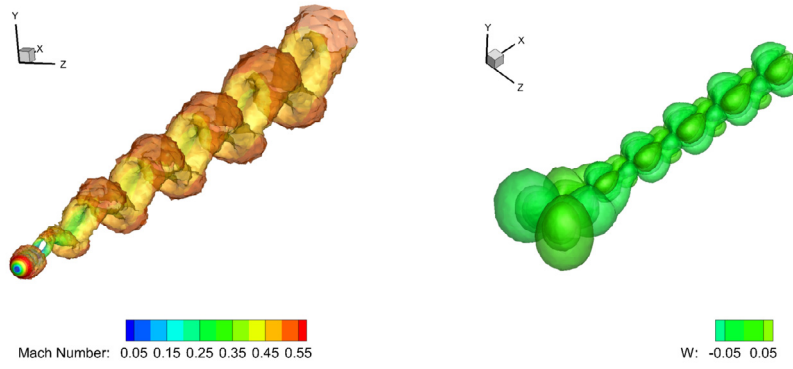


Fig. 18. Vortical structure and streamwise velocity iso-surfaces at $t = 282$ s for the laminar flow past a sphere.

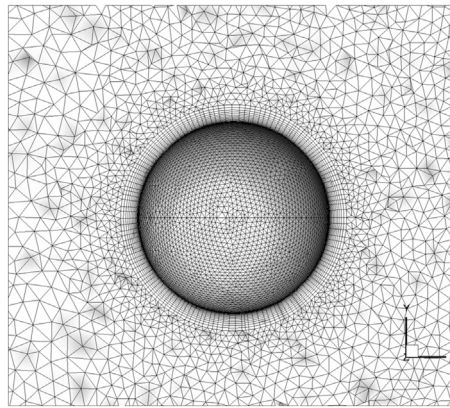


Fig. 19. Cutaway of the unstructured mesh for the turbulent flow around a sphere close to the boundary layer.

4.4. Turbulent flow past a sphere

Simulations were also performed for the turbulent flow around a sphere at $M_\infty = 0.2$ and $Re = 10,000$ [65]. A hybrid unstructured mesh was used consisting of 2,724,453 elements, where the boundary layer region was discretized by prisms and the rest of the domain by tetrahedral elements (Fig. 19). The computational domain has dimensions $(x, y, z) \in [0, 50] \times [0, 20] \times [0, 20]$, with the sphere centre located at $[10.5, 10, 10]$. No-slip was applied on the surface of the sphere and free-stream values elsewhere in the boundaries of the computational domain. Similar to the laminar flow, the WENO-3rd order scheme was employed and the CFL number was 0.28. The simulation was run up to time $t = 308$ s in order to obtain the flow statistics.

The time history of the drag coefficient is shown in Fig. 20. The average drag coefficient is 0.402. This value is in close agreement with the experimental data of [65] and the numerical results of [67,68], as well as the references therein (Table 3). The velocity oscillations in the wake of the sphere are shown in Fig. 20 at the position $(15.5, 10, 10)$.

In Fig. 21 the oblique view of the iso-surfaces of the vortical structure coloured by the Mach number provides a good view of the flow in the turbulent regime. The flow remains laminar ahead of the equator and separates after, featuring small-scale vortices in the wake of the sphere, which is typical for this Reynolds number [65]. The Q criterion was used to show the vortical wake structures Fig. 22. In the turbulent case, the position of the vortex roll-up is closer to the sphere compared to the laminar flow [65].

4.5. Shock-wave boundary-layer interaction (SWBLi)

Assessment of the present methods in high-speed viscous flows was performed for the experiment of Schülein [69] concerning an incoming flow of Mach number $M_\infty = 5.0$ that collides with a shock generator at an angle $\beta = 10^\circ$. The incident shock impinges on the lower flat plate agitating the turbulent boundary layer and forming a separation zone. The boundary layer reattaches further downstream where fluctuations are induced due to the presence of compression waves and expansion fans. The Reynolds number is $Re = 37 \times 10^6 / m$, thus prohibiting, in terms of computational cost, the use of LES. Therefore, simulations were performed in the RANS framework.

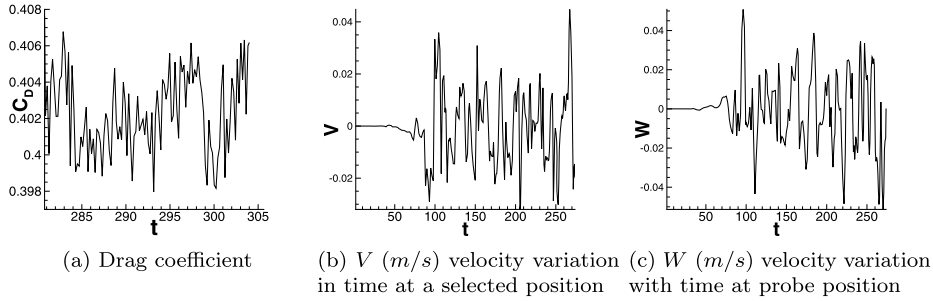


Fig. 20. Time history of drag coefficient and variation of V (m/s) and W (m/s) velocity in time at a selected position (15.5, 10, 10) for the turbulent flow around a sphere.

Table 3

Drag coefficients for the turbulent flow around a sphere at $Re = 10,000$. Comparisons are shown with the experiments of Achenbach [65] and LES computations of Constantinescu and Squires [67] and Yun et al. [68].

	C_D	Turbulence model
Achenbach [65]	0.4	—
Yun et al. [68]	0.393	LES
Constantinescu and Squires [67]	0.393	LES
Present	0.4028	ILES Unstructured

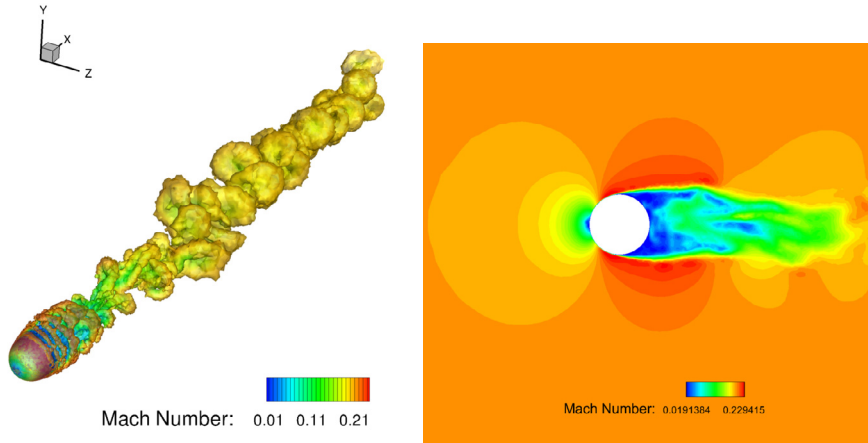


Fig. 21. Vortical iso-surfaces coloured by Mach number using the Q criterion and Mach contour at the xy -plane at $t = 272$ s for the turbulent flow around a sphere.

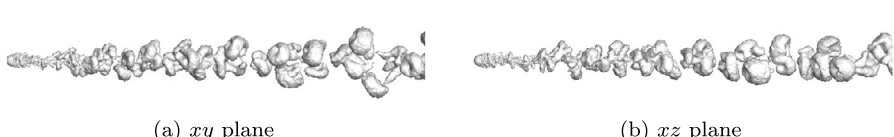


Fig. 22. Vorticity iso-surfaces at $t = 272$ s for the turbulent flow around a sphere.

Current numerical methods and turbulence models poorly predict wall shear stresses and exerted forces compared with experimental data, with the error notably increasing in the disturbed boundary layer region. Generally, the numerical vs experimental differences in the skin friction of SWBLI flows are more profound in high Reynolds numbers RANS simulations [70]. At lower Reynolds numbers, where LES is feasible, the numerical results are in better agreement with experiments [71]. Previous studies employing RANS models for SWBLI at high Reynolds number flows looked at modifications of turbulence models by incorporating additional terms to ameliorate the predictions in the supersonic regime [72,73].

As steady-state solutions are considered and the flow is symmetric along the spanwise direction, two-dimensionality (x, y) can be assumed and local time stepping is employed for accelerating numerical convergence. The Spalart–Allmaras

(SA) turbulence model [74] is employed to predict the production, transport, diffusion and destruction of the turbulent eddy viscosity. The model solves one transport equation for a turbulent parameter \tilde{v} which is related to eddy viscosity μ_t :

$$\mu_t = \rho \tilde{v} f_{v1} \quad \text{where } f_{v1} = \frac{(\rho \tilde{v} / \mu_l)^3}{(\rho \tilde{v} / \mu_l)^3 + C_{v1}^3} \quad \text{and } C_{v1} = 7.1. \quad (48)$$

The SA transport equation turbulence model is written in conservative form as

$$\frac{\partial(\rho \tilde{v})}{\partial t} + \nabla \cdot \rho \tilde{v} \mathbf{u} = C_{b1} \tilde{S} \rho \tilde{v} + \frac{1}{\sigma} (\nabla \cdot (\mu_l + \rho \tilde{v}) \nabla \tilde{v}) + \frac{1}{\sigma} C_{b2} (\nabla \tilde{v} \cdot \nabla \tilde{v}) - C_{w1} f_w \rho \left(\frac{\tilde{v}}{d} \right)^2 \quad (49)$$

where d is the distance of the cell centre from the nearest wall; boundary layer transition terms are excluded; and \tilde{S} is given by

$$\tilde{S} = \Omega + f_{v2} \frac{\tilde{v} \rho}{k^2 d^2} \quad \text{where } \Omega = \sqrt{\omega \cdot \omega} \text{ and } f_{v2} = 1 - \frac{\rho \tilde{v} / \mu_l}{1 + f_{v1}(\rho \tilde{v} / \mu_l)} \quad (50)$$

where, ω is the vorticity vector, and f_w is obtained as follows

$$f_w = g \left(\frac{1 + C_{w3}^6}{g^6 + C_{w3}^6} \right)^{1/6} \quad \text{where } g = r + C_{w2}(r^6 - r) \text{ and } r = \min \left[\frac{\tilde{v}}{\tilde{S} k^2 d^2}, 10 \right] \quad (51)$$

with the closure constants being

$$\begin{aligned} C_{b2} &= 0.622, & C_{w1} &= \frac{C_{b1}}{\kappa^2} + \frac{1 + C_{b2}}{\sigma}, & C_{w2} &= 0.3, \\ C_{b1} &= 0.1355, & C_{w3} &= 2.0, & \sigma &= 2/3, & \kappa &= 0.41. \end{aligned} \quad (52)$$

An initial value for the turbulence parameter is set as $\tilde{v}_\infty = 3.0 v_{laminar}$; at the wall \tilde{v} is zero. A mixed-element grid comprising 178,116 elements, corresponding to $y^+ \approx 1$, is employed; Fig. 24(a) illustrates the computational domain.

The benefits of high-order discretisation of the viscous terms by reconstructing the gradients of velocities and temperature with the single quadrature constrained least-square method at the wall are investigated against the relatively simpler cell-centred based Green–Gauss method [75]. The Green–Gauss (GG) method computes the gradients at the centre of the element using the cell-centred value from its direct side neighbours by averaging and integrating around the boundary of the considered element. The gradient of a conserved variable u_i is given by

$$\nabla u_i = \frac{1}{|V|} \sum_{j=1}^L \frac{1}{2} (u_i + u_j) \mathbf{n}_{x,y} |A_j|. \quad (53)$$

The computed gradient by the Green–Gauss method is more grid-dependent than the least-square method, and potentially can affect the overall accuracy at the highly skewed elements near the wall (aspect ratio of 10^3 in the present test case) by producing unphysical spikes and under/over estimated solutions. This trend can be depicted in Fig. 25 where the computed skin-friction coefficients C_f for both MUSCL-TVD and WENO schemes with the GG method are notably underpredicted compared to the least-square, even upstream in the undisturbed boundary layer. The proposed constrained least-square reconstruction for the gradients of the viscous terms is superior to GG method, at least in terms of accuracy since the same order of polynomial is used as for the inviscid terms.

The separation zone formed under the λ -shock encompasses unsteadiness, which is attributed to three-dimensionality as well as the formation of spanwise Taylor–Gortler vortices. Even though the original experimental apparatus is three-dimensional, the two-dimensional model adequately captures the shock structure as shown in Fig. 23(a) and (b), with the separation and reattachment locations satisfactorily predicted. In all the test cases examined so far the same value of linear weight $d_0 = 10^3$ has been used for the central stencil of WENO schemes. Although this may seem odd for the present test case since we are dealing with a flow problem governed by shocks and strong gradients, it is the non-linear weight that influences the reconstruction, based on the smoothness indicators of the solution which can be orders of magnitude greater than the linear weight across discontinuities. In Fig. 23(c) the central stencil non-linear WENO weight assigned for each cell can be seen. It can be noticed that in smooth regions of the flow the central stencil has the greatest influence in the reconstruction, corresponding to a non-linear WENO weight close to 1.0. In regions of sharp gradients the opposite is, however, true, i.e. the directional stencils have the greatest influence in the reconstruction.

The separation and reattachment locations can be better interpreted from the skin-friction plots (Fig. 25(a)), where the WENO-3rd order in conjunction with the least-square method provides the best agreement with the experiment. Furthermore, the C_f predictions using the WENO scheme reach a higher plateau downstream of the separation zone, thus improving the agreement with the experimental data. The advantages of using WENO schemes is also obvious for the wall pressure predictions (Fig. 25(b)), where the wall pressure recovers with higher values, capturing the impinging shock with a sharper profile and damping the spurious oscillations presented in the MUSCL-TVD solution.

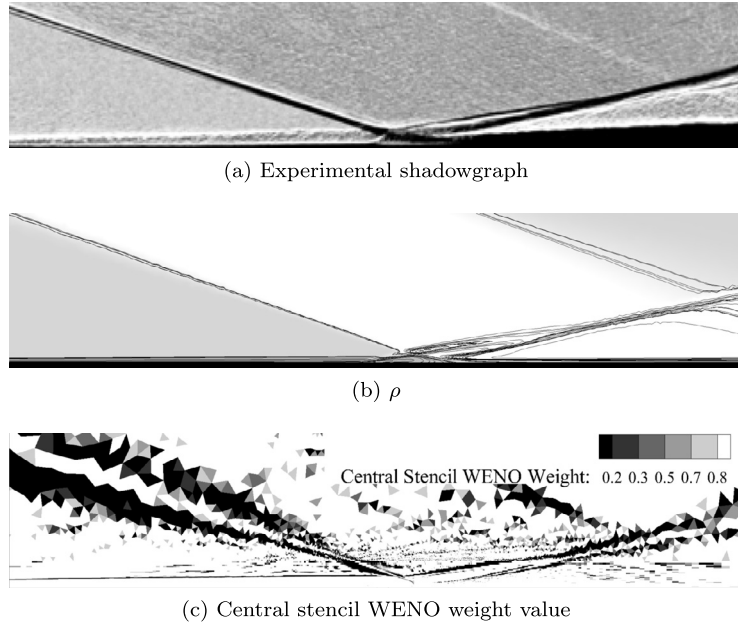


Fig. 23. Spark shadowgraph visualisation from the experiment [69], computed contours and lines of density ρ , and central stencil WENO weight value for the 3rd-order WENO scheme with the least-square gradient method ($M_\infty = 5.0$, $\beta = 10^\circ$ and $Re = 37 \times 10^6/\text{m}$).

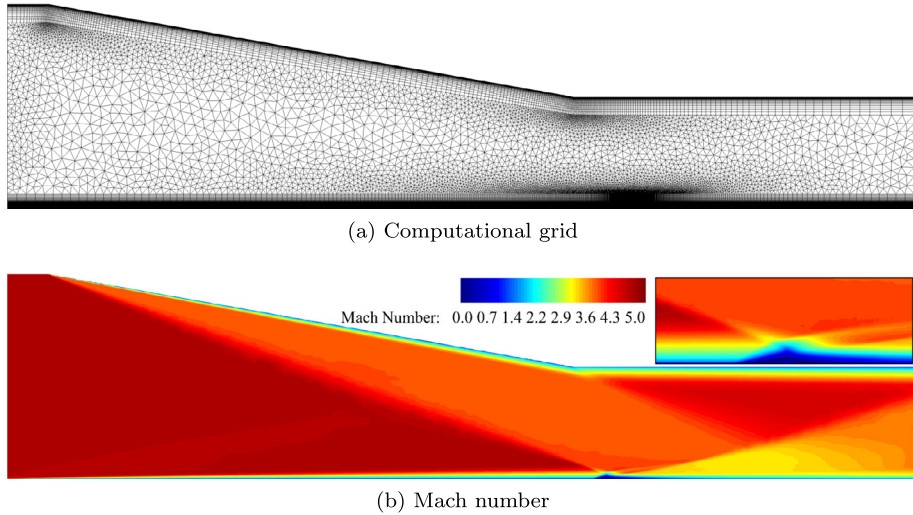


Fig. 24. Computational grid and Mach number contours employing the WENO-3rd order schemes with the least-square gradient reconstruction ($M_\infty = 5.0$, $\beta = 10^\circ$ and $Re = 37 \times 10^6/\text{m}$).

5. Concluding remarks

WENO schemes were implemented in viscous flows at different Reynolds numbers and their accuracy and efficiency were assessed against experimental and other numerical results. The key findings of the present paper are summarised below:

- The numerical dissipation of WENO schemes varies not only with the grid resolution, but also with the arbitrariness of shape and orientation of elements, as well as with the compactness of the directional stencils in the unstructured mesh.
- The present results showed that a uniform straight-sided elements mesh does not necessarily provide the best results since the corresponding WENO stencils are not as compact as in an equivalent tetrahedral mesh. It also seems that the arbitrariness in shape and orientation of elements in an unstructured mesh benefits flows characterised by chaotic/turbulent behaviour, though the exact mechanism is not yet understood.

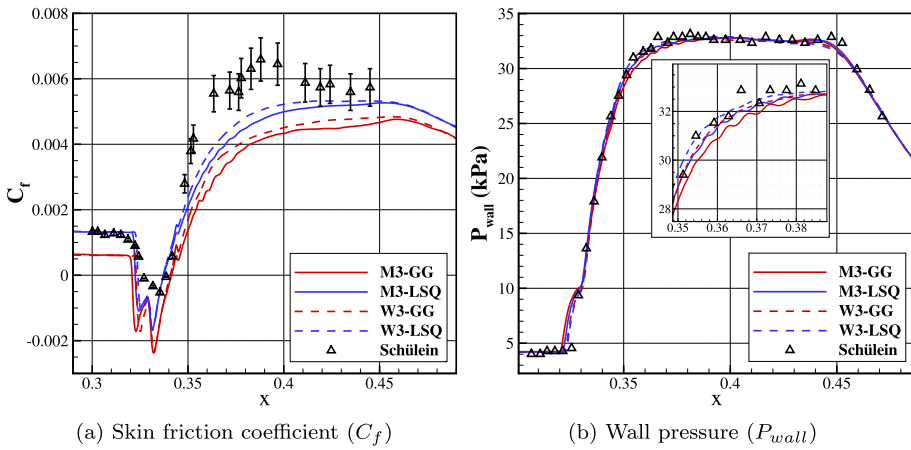


Fig. 25. Coefficient of skin friction C_f and wall pressure P_{wall} employing the MUSCL-TVD 3rd-order (M3) and WENO-3rd order (W3) schemes with the Green-Gauss (GG) and least-square (LSQ) viscous gradient reconstruction methods compared with Schülein experimental data [69] ($M_\infty = 5.0$, $\beta = 10^\circ$ and $Re = 37 \times 10^6/m$).

- The WENO schemes are computationally expensive but the WENO-3rd order scheme provides the best results in terms of accuracy and computational cost in comparison with WENO-5th and MUSCL-2nd order methods.
 - The higher-order WENO schemes showed better scalability performance compared to second-order schemes.
 - The performance the subject WENO schemes is also demonstrated in the SWBLI flow problem, where their robustness and accuracy provide additional benefits in the context of RANS simulations.
 - The presented constrained least-square reconstruction for the gradients of the viscous terms is superior in terms of accuracy compared to a Green-Gauss gradient estimation method, as assessed in the SWBLI test problem and can be considered quite natural way of computing the gradients of viscous terms with the same order polynomials as for the inviscid terms.

Further investigation of the schemes in the context of hybrid RANS–ILES is under-development and results will be presented in a future paper.

Acknowledgements

The authors acknowledge the computing time on the UK national high-performance computing service HECToR that was provided through the UK Turbulence Consortium in the framework of the EPSRC grant EP/G069581/1. The authors would also like to thank Charles Moulinec and David Emerson at Daresbury Laboratory for their support and advice regarding the implementation of the code to the HECToR UK National Supercomputing Service facility. The authors would also like to acknowledge the constructive comments, and suggestions provided by the anonymous reviewers that greatly improved the quality of the article.

References

- [1] R. Abgrall, On essentially non-oscillatory schemes on unstructured meshes: analysis and implementation, *J. Comput. Phys.* 114 (1) (1994) 45–58.
 - [2] M. Ciardi, P. Sagaut, M. Klein, W. Dawes, A dynamic finite volume scheme for large-eddy simulation on unstructured grids, *J. Comput. Phys.* 210 (2) (2005) 632–655.
 - [3] M. Dumbsar, M. Kaser, V. Titarev, E. Toro, Quadrature-free non-oscillatory finite volume schemes on unstructured meshes for nonlinear hyperbolic systems, *J. Comput. Phys.* 226 (1) (2007) 204–243.
 - [4] O. Friedrich, Weighted essentially non-oscillatory schemes for the interpolation of mean values on unstructured grids, *J. Comput. Phys.* 144 (1) (1998) 194–212.
 - [5] A. Haselbacher, A WENO reconstruction algorithm for unstructured grids based on explicit stencil construction, in: 43rd AIAA Aerospace Sciences Meeting and Exhibit—Meeting Papers, 2005, pp. 3369–3378.
 - [6] R. Abgrall, G. Baurin, P. Jacq, M. Ricchiuto, Some examples of high order simulations parallel of inviscid flows on unstructured and hybrid meshes by residual distribution schemes, *Comput. Fluids* 61 (2012) 6–13.
 - [7] R. Abgrall, A. Larat, M. Ricchiuto, Construction of very high order residual distribution schemes for steady inviscid flow problems on hybrid unstructured meshes, *J. Comput. Phys.* 230 (11) (2011) 4103–4136.
 - [8] G. Hu, R. Li, T. Tang, A robust WENO type finite volume solver for steady Euler equations on unstructured grids, *Commun. Comput. Phys.* 9 (3) (2011) 627–648.
 - [9] G. Lei, W. Li, Y. Ren, High-order unstructured-grid WENO FVM for compressible flow computation, *Jisuan WuLi/Chin. J. Comput. Phys.* 28 (5) (2011) 633–640.
 - [10] W. Li, Y. Ren, Quadrature-free non-oscillation finite volume scheme for solving Navier–Stokes equations on unstructured grids, in: AIP Conf. Proc., vol. 1376, 2011, pp. 639–641.

- [11] X. Nogueira, L. Cueto-Felgueroso, I. Colominas, F. Navarrina, M. Casteleiro, A new shock-capturing technique based on moving least squares for higher-order numerical schemes on unstructured grids, *Comput. Methods Appl. Mech. Eng.* 199 (37–40) (2010) 2544–2558.
- [12] C. Ollivier-Gooch, Quasi-ENO schemes for unstructured meshes based on unlimited data-dependent least-squares reconstruction, *J. Comput. Phys.* 133 (1) (1997) 6–17.
- [13] C.O. Gooch, M.V. Altena, A high-order-accurate unstructured mesh finite-volume scheme for the advection–diffusion equation, *J. Comput. Phys.* 181 (2) (2002) 729–752.
- [14] R. Rossi, Direct numerical simulation of scalar transport using unstructured finite-volume schemes, *J. Comput. Phys.* 228 (5) (2009) 1639–1657.
- [15] V. Titarev, P. Tsoutsanis, D. Drikakis, WENO schemes for mixed-element unstructured meshes, *Commun. Comput. Phys.* 8 (3) (2010) 585–609.
- [16] P. Tsoutsanis, V. Titarev, D. Drikakis, WENO schemes on arbitrary mixed-element unstructured meshes in three space dimensions, *J. Comput. Phys.* 230 (4) (2011) 1585–1601.
- [17] W. Wolf, J. Azevedo, High-order ENO and WENO schemes for unstructured grids, *Int. J. Numer. Methods Fluids* 55 (10) (2007) 917–943.
- [18] J. Zhu, J. Qiu, Local DG method using WENO type limiters for convection–diffusion problems, *J. Comput. Phys.* 230 (11) (2011) 4353–4375.
- [19] B. Cockburn, C.-W. Shu, Runge–Kutta discontinuous Galerkin methods for convection-dominated problems, *J. Sci. Comput.* 16 (3) (2001) 173–261.
- [20] M. Dumbser, D. Balsara, E. Toro, C.-D. Munz, A unified framework for the construction of one-step finite volume and discontinuous Galerkin schemes on unstructured meshes, *J. Comput. Phys.* 227 (18) (2008) 8209–8253.
- [21] G. Gassner, F. Lorcher, C.-D. Munz, A discontinuous Galerkin scheme based on a space–time expansion ii. viscous flow equations in multi dimensions, *J. Sci. Comput.* 34 (3) (2008) 260–286.
- [22] Z. Xu, Y. Liu, C.-W. Shu, Hierarchical reconstruction for discontinuous Galerkin methods on unstructured grids with a WENO-type linear reconstruction and partial neighboring cells, *J. Comput. Phys.* 228 (6) (2009) 2194–2212.
- [23] J. Zhu, J. Qiu, C.-W. Shu, M. Dumbser, Runge–Kutta discontinuous Galerkin method using WENO limiters II: Unstructured meshes, *J. Comput. Phys.* 227 (9) (2008) 4330–4353.
- [24] J. Zhu, J. Qiu, Runge–Kutta discontinuous Galerkin method using WENO-type limiters: Three-dimensional unstructured meshes, *Commun. Comput. Phys.* 11 (3) (2012) 985–1005.
- [25] M. Dumbser, Arbitrary high order PNPM schemes on unstructured meshes for the compressible Navier–Stokes equations, *Comput. Fluids* 39 (1) (2010) 60–76.
- [26] Y. Zhou, Z. Wang, Implicit large eddy simulation of transitional flow over a SD7003 wing using high-order spectral difference method, in: 40th AIAA Fluid Dynamics Conference, 2010, art. no. 2010-4442.
- [27] Z. Xu, Y. Liu, C.-W. Shu, Hierarchical reconstruction for spectral volume method on unstructured grids, *J. Comput. Phys.* 228 (16) (2009) 5787–5802.
- [28] Y. Sun, Z. Wang, Y. Liu, Spectral (finite) volume method for conservation laws on unstructured grids VI: Extension to viscous flow, *J. Comput. Phys.* 215 (1) (2006) 41–58.
- [29] D. Stanescu, W. Habashi, Essentially nonoscillatory Euler solutions on unstructured meshes using extrapolation, *AIAA J.* 36 (8) (1998) 1413–1416.
- [30] G.S. Jiang, C.W. Shu, Efficient implementation of weighted ENO schemes, *J. Comput. Phys.* 126 (1) (1996) 202–228.
- [31] J. Shi, C. Hu, C.-W. Shu, A technique of treating negative weights in WENO schemes, *J. Comput. Phys.* 175 (1) (2002) 108–127.
- [32] C.-W. Shu, S. Osher, Efficient implementation of essentially non-oscillatory shock-capturing schemes, *J. Comput. Phys.* 77 (2) (1988) 439–471.
- [33] F.F. Grinstein, L.G. Margolin, W.J. Rider, *Implicit Large Eddy Simulation: Computing Turbulent Fluid Dynamics*, Cambridge University Press, 2011.
- [34] J. Domaradzki, Z. Xiao, P. Smolarkiewicz, Effective eddy viscosities in implicit large eddy simulations of turbulent flows, *Phys. Fluids* 15 (12) (2003) 3890–3893.
- [35] D. Drikakis, M. Hahn, A. Mosedale, B. Thornber, Large eddy simulation using high-resolution and high-order methods, *Philos. Trans. R. Soc. A, Math. Phys. Eng. Sci.* 367 (1899) (2009) 2985–2997.
- [36] C. Fureby, F. Grinstein, Monotonically integrated large eddy simulation of free shear flows, *AIAA J.* 37 (5) (1999) 544–556.
- [37] M. Galbraith, M. Visbal, Implicit large eddy simulation of low Reynolds number flow past the SD7003 airfoil, in: 46th AIAA Aerospace Sciences Meeting and Exhibit, 2008.
- [38] K. Ishiko, N. Ohnishi, K. Ueno, K. Sawada, Implicit large eddy simulation of two-dimensional homogeneous turbulence using weighted compact non-linear scheme, *J. Fluids Eng.* 131 (6) (2009) 0614011–06140114.
- [39] A. Uranga, P.-O. Persson, M. Drela, J. Peraire, Implicit large eddy simulation of transition to turbulence at low Reynolds numbers using a discontinuous Galerkin method, *Int. J. Numer. Methods Eng.* 87 (1–5) (2011) 232–261.
- [40] M. Hahn, D. Drikakis, Implicit large eddy simulation of turbulent flows using high-resolution methods, in: 43rd AIAA Aerospace Sciences Meeting and Exhibit—Meeting Papers, 2005, pp. 4973–4977.
- [41] Y. Shimada, B. Thornber, D. Drikakis, High-order implicit large eddy simulation of gaseous fuel injection and mixing of a bluff body burner, *Comput. Fluids* 44 (1) (2011) 229–237.
- [42] B. Thornber, A. Mosedale, D. Drikakis, On the implicit large eddy simulations of homogeneous decaying turbulence, *J. Comput. Phys.* 226 (2) (2007) 1902–1929.
- [43] M. Dumbser, M. Kaser, Arbitrary high order non-oscillatory finite volume schemes on unstructured meshes for linear hyperbolic systems, *J. Comput. Phys.* 221 (2) (2007) 693–723.
- [44] M.S. Shephard, M.K. Georges, Automatic three-dimensional mesh generation by the finite octree technique, *Int. J. Numer. Methods Eng.* 32 (4) (1991) 709–749.
- [45] M.A. Yerry, M.S. Shephard, Automatic three-dimensional mesh generation by the modified-OCTREE technique, *Int. J. Numer. Methods Eng.* 20 (11) (1984) 1965–1990.
- [46] Y.T. Zhang, C.W. Shu, Third order WENO scheme on three dimensional tetrahedral meshes, *Commun. Comput. Phys.* 5 (2–4) (2008) 836–848.
- [47] A. Harten, B. Engquist, S. Osher, S. Chakravarthy, Uniformly high order accurate essentially non-oscillatory schemes, III, *J. Comput. Phys.* 71 (2) (1987) 231–303.
- [48] E.F. Toro, *Riemann Solvers and Numerical Methods for Fluid Dynamics – A Practical Introduction*, Springer-Verlag, Berlin, 1997.
- [49] G. Gassner, C.-D. Lorcher, F. Munz, A contribution to the construction of diffusion fluxes for finite volume and discontinuous Galerkin schemes, *J. Comput. Phys.* 224 (2) (2007) 1049–1063.
- [50] M. Brachet, U. Frisch, D. Meiron, S. Orszag, B. Nickel, R. Morf, Small-scale structure of the Taylor–Green vortex, *J. Fluid Mech.* 130 (1983) 411–452.
- [51] D. Drikakis, C. Fureby, F. Grinstein, D. Youngs, Simulation of transition and turbulence decay in the Taylor–Green vortex, *J. Turbul.* 8 (2007) 1–12.
- [52] C.-W. Shu, W.-S. Don, D. Gottlieb, O. Schilling, L. Jameson, Numerical convergence study of nearly incompressible, inviscid Taylor–Green vortex flow, *J. Sci. Comput.* 24 (1) (2005) 569–595.
- [53] A. Mosedale, D. Drikakis, Assessment of very high order of accuracy in implicit LES models, *J. Fluids Eng.* 129 (12) (2007) 1497–1503.
- [54] F. Grinstein, D. Drikakis, Computing turbulent flow dynamics with implicit large eddy simulation, *J. Fluids Eng.* 129 (12) (2007) 1481–1482.
- [55] D. Drikakis, Advances in turbulent flow computations using high-resolution methods, *Prog. Aerosp. Sci.* 39 (6–7) (2003) 405–424.
- [56] M. Hahn, D. Drikakis, Large eddy simulation of compressible turbulence using high-resolution methods, *Int. J. Numer. Methods Fluids* 47 (8–9) (2005) 971–977.
- [57] B. Thornber, D. Drikakis, Implicit large-eddy simulation of a deep cavity using high-resolution methods, *AIAA J.* 46 (10) (2008) 2634–2645.

- [58] B. Zhong, F. Scheurich, V. Titarev, D. Drikakis, Turbulent flow simulations around a multi-element airfoil using URANS, DES and ILES approaches, in: 19th AIAA Computational Fluid Dynamics Conference, 2009, art. no. 2009-3799.
- [59] S. Hickel, N. Adams, J. Domaradzki, Letter to the editor: On the evolution of dissipation rate and resolved kinetic energy in ALDM simulations of the Taylor–Green flow, *J. Comput. Phys.* 229 (6) (2010) 2422–2423.
- [60] J. Jinhee, F. Hussain, On the identification of a vortex, *J. Fluid Mech.* 285 (1995) 69–94.
- [61] G. Karypis, V. Kumar, Multilevel k-way partitioning scheme for irregular graphs, *J. Parallel Distrib. Comput.* 48 (1998) 96–129.
- [62] T. Johnson, V. Patel, Flow past a sphere up to a Reynolds number of 300, *J. Fluid Mech.* 378 (1999) 19–70.
- [63] A. Tomboulides, S. Orszag, Numerical investigation of transitional and weak turbulent flow past a sphere, *J. Fluid Mech.* 416 (2000) 45–73.
- [64] R. Mittal, Planar symmetry in the unsteady wake of a sphere, *AIAA J.* 37 (2–3) (1999) 388–390.
- [65] E. Achenbach, Effects of surface roughness and tunnel blockage on the flow past spheres, *J. Fluid Mech.* 65 (Part 1) (1974) 113–125.
- [66] P. Bagchi, S. Balachandar, Steady planar straining flow past a rigid sphere at moderate Reynolds number, *J. Fluid Mech.* 466 (2002) 365–407.
- [67] G. Constantinescu, K. Squires LES, Investigations of turbulent flow over a sphere at $Re = 10,000$, *Flow Turbul. Combust.* 70 (1–4) (2003) 267–298.
- [68] G. Yun, D. Kim, H. Choi, Vortical structures behind a sphere at subcritical Reynolds numbers, *Phys. Fluids* 18 (015102) (2006) 1–14.
- [69] E. Schülein, Skin-friction and heat flux measurements in shock/boundary-layer interaction flows, *AIAA J.* 44 (8) (2006) 1732–1741.
- [70] G. Gerolymos, E. Sauret, I. Vallet, Oblique-shock-wave/boundary-layer interaction using near-wall Reynolds stress models, *AIAA J.* 42 (6) (2004) 1089–1100.
- [71] M. Grilli, P.J. Schmid, S. Hickel, N.A. Adams, Analysis of unsteady behaviour in shockwave turbulent boundary layer interaction, *J. Fluid Mech.* 700 (2012) 16–28.
- [72] X. Xiao, H.A. Hassan, J.R. Edwards, R.L. Gaffney Jr., Role of turbulent Prandtl numbers on heat flux at hypersonic Mach numbers, *AIAA J.* 45 (4) (2007) 806–813.
- [73] A. Ali Pasha, K. Sinha, Shock-unsteadiness model applied to oblique shock wave/turbulent boundary-layer interaction, *Int. J. Comput. Fluid Dyn.* 22 (8) (2008) 569–582.
- [74] P.R. Spalart, S.R. Allmaras, One-equation turbulence model for aerodynamic flows, *Rech. Aéronaut.* 1 (1994) 5–21.
- [75] T. Barth, D. Jespersen, The design and application of upwind schemes on unstructured meshes, in: AIAA, Aerospace Science Meeting 1989-0366, <http://dx.doi.org/10.2514/6.1989-366>.